Journal of Computational Design and Engineering Vol. 1, No. 3 (2014) 194~201
www.jcde.org

Automated quality characterization of 3D printed bone scaffolds

Tzu-Liang Bill Tseng[1], Aditya Chilukuri[1], Sang C. Park[2] and Yongjin James Kwon[2,*]

[1] *Department of Industrial, Manufacturing and Systems Engineering, The University of Texas at El Paso, El Paso, TX 79968, USA*
[2] *Department of Industrial Engineering, Ajou University, Suwon, South Korea,*

(Manuscript Received February 4, 2014; Revised May 12, 2014; Accepted May 12, 2014)

Abstract

Optimization of design is an important step in obtaining tissue engineering scaffolds with appropriate shapes and inner microstructures. Different shapes and sizes of scaffolds are modeled using UGS NX 6.0 software with variable pore sizes. The quality issue we are concerned is the scaffold porosity, which is mainly caused by the fabrication inaccuracies. Bone scaffolds are usually characterized using a scanning electron microscope, but this study presents a new automated inspection and classification technique. Due to many numbers and size variations for the pores, the manual inspection of the fabricated scaffolds tends to be error-prone and costly. Manual inspection also raises the chance of contamination. Thus, non-contact, precise inspection is preferred. In this study, the critical dimensions are automatically measured by the vision camera. The measured data are analyzed to classify the quality characteristics. The automated inspection and classification techniques developed in this study are expected to improve the quality of the fabricated scaffolds and reduce the overall cost of manufacturing.

Keywords: Bone scaffolds; Automated inspection; 3D print; Classification; Regression model; Neural networks

1. Introduction

An ideal bone implant should have the same structure and similar composition as the bone. One of the approaches includes production of implants using scaffolds [1, 2]. The shape and architecture of scaffolds are important as they support the cells and produce extracellular matrix to generate new tissues. Scaffold should have the same shape as the defective bone, in order to be placed well in a body and guide bone's growth correctly [1, 2]. Traditionally, fabrication methods, such as fiber bonding, solvent casting, particulate leaching, membrane lamination, melt molding, gas forming, and cryogenic induced phase separations, have been employed [1, 2]. Those techniques are also based on manual works, hence extra procedures are associated with in terms of getting suitable shapes and microstructures. However, the extra steps are not easy since they cannot be controlled well. To overcome limitations with the traditional fabrication techniques, the rapid prototyping (RP) has been explored by many scientists. RP technologies enable us to provide scaffolds with well-defined and controlled internal architecture. The RP technologies, including stereo lithography (SLA), selective laser sintering (SLS), fused deposition modeling (FDM), three-dimensional printing (TDP or 3DP), have been widely applied in fabricating bionic scaffolds for tissue engineering [3]. Dimensional accuracy is limited in these processes by the nozzle size and laser diameter, control over the print head, laser movement and positioning, and the particle size of the powder. 3D printing is one prospective RP technique that may be used in manufacturing hard tissues. The 3DP, SLS and FDM represent the most promising techniques that can be used in hard tissue manufacturing.

In tune with the RP technologies, various biomaterials and other fabrication techniques have been tested for bone tissue engineering. Liu et al. [4] published a review of polymer materials, scaffold design, fabrication techniques, and the architectural parameters of the scaffold. Though other factors like cell sources, regulating molecules, mechanical stimulation, bioreactor design, cultivation conditions and clinical considerations are important for the successful tissue development, they are not discussed in this paper. Natural polymers have the advantage of biological recognition, but are limited with respect to the mechanical properties and biodegradability. These facts compelled researchers to try synthetic polymers. Gbureck et al. [5] attempted to manufacture custom-made calcium pyrophosphate implant structures and scaffolds through the 3D powder printing process. Samples were prepared using the powders and the diluted phosphoric acid with different concentrations from 5% to 30%. Layer thickness of 100 μm and binder-volume ratio of 0.28 for shell and 0.14 for core with a saturation level of 89%, were adopted for printing. Surfaces of failed samples were examined

*Corresponding author. Tel.: +82-31-219-2418, Fax.: +82 -31-219-1610
E-mail address: yk73@ajou.ac.kr

doi: 10.7315/JCDE.2014.019

using a scanning electron microscope. Printing process allowed a production of components with a resolution of ± 200 μm. Leukers et al. [6] focused on the evaluation of the seeded scaffolds that were manufactured with 3D printing technology. A special scaffold was designed to maximize the surface and facilitate the seeding process to enhance cell adhesion and supply of nutrients. Spray dried hydroxyapatite (HA) granulates containing polymeric additives and water soluble polymer blends were used. Powder-based 3D printing process was found to induce the micro porosity, which increases the surface accessibility of the scaffold for fluid medium. From the above findings, HA scaffolds made by 3D printing seem to be highly suitable for bone tissue engineering. Khalyfa et al. [7] developed a powder mixture comprising tetra calcium phosphate (TTCP) as reactive components and β-tricalcium phosphate or calcium sulphate as biodegradable fillers. The mixture could be used for bone repair applications in load bearing areas. The above works used sophisticated equipment for characterization, such as a scanning electron microscope [8].

This research automates the surface feature inspection of bone scaffolds using an automated vision technology. The inspection of bone scaffolds is generally performed using a scanning electron microscope and the characterization process is manual. To avoid human intervention and common errors, the process can be automated using advanced sensors and inspection devices. Sensors such as machine vision cameras are much faster and accurate than manual inspection. By activating suitable image processing algorithms for given dimensions, the whole characterization process can be completed in less than a minute. Efforts are also made to increase the capacity of the camera by extending the lens of the camera with a microscope lens. The images of size less than 500 μm can be analyzed with ease. Since bone scaffolds contain many pores on the surface, the accurate measurement and characterization of surface features are crucial. The inspection data obtained by the vision system are analyzed using multi-layer perceptron neural networks and radial basis function networks for classification. Regression analysis is also carried out to gauge the prediction accuracy. The performance of developed models is presented as well.

The structure of this paper is as follows. The first section is an introduction, which delineates the definition of bone scaffold, 3D printing, and also provides the review of related materials. Section 2 elaborates on the research methodology, while the design and fabrication of 3D parts are presented in Section 3. Data analysis is illustrated in Section 4. The conclusion is drawn in Section.

2. Research methodology

The methodology for this research consists of two distinctive phases. Phase I is a classification analysis by neural networks using Statistica 9. The results of classification obtained from both multilayer perceptron (MLP) and radial basis function (RBF) networks are compared. Phase II is a regression analysis on the prediction of porosity. In Phase II, error terms from the models are compared to assess the prediction accuracy of porosity.

2.1 Design selection

Tissue engineering generally requires the use of a porous, bio-resorbable scaffold, which serves as a three-dimensional (3D) template for the initial cell attachment and subsequent tissue formation, both in vitro and in vivo. Ideally, a scaffold should have the following characteristics: (1) a suitable macrostructure to promote cell proliferation and cell-specific matrix production; (2) an open-pore geometry with a highly porous surface and microstructure that enables cell growth; (3) optimal pore size for tissue regeneration and to avoid pore occlusion; and (4) suitable surface morphology and physiochemical properties to encourage intracellular signaling and recruitment of cells [1-8]. Experiments reveal that the porosity of scaffolds, which is manufactured by the FDM RP machines, depends on four main parameters. Those include slice thickness, road width, raster gap, and raster angle. The slice thickness is the thickness of the layer used to build the model layer-by-layer. The road width is the width of the extruded layer. The raster gap is the gap between the laying roads within a sliced plane of the part. The raster angle is the angle between the succeeding horizontal raster layers of the model. The experimental value of the porosity P can be calculated by the equation [1-8]:

$$P = \left[1 - \left(\frac{v_t}{v_a}\right)\right] \tag{1}$$

where v_a = apparent volume (total volume) of the model, and v_t = true volume of the model (volume occupied by material). We assume that large porosity for vascularization is of prime importance, as long as both scaffold and tissue stiffness are maintained within an acceptable range. The optimization problem denoted as the porosity design can be written as [1-8]:

$$Objective\ Function = \max_{E^{scaffols}}\left(\frac{1 - v_a}{v_t}\right) \tag{2}$$

where $E^{scaffold}$ = Young's Modulus of scaffold base material, and d_1 = pore diameter. We propose the relationship between void volume components, structural material properties, and dominant design characteristics, which govern the strength of porous architecture. The basic demand of tissue engineered scaffolds is that they should be porous enough to support interconnectivity that has been demonstrated to be around 60% porosity by volume. We consider two shapes of scaffold pores, including (1) the basic circular shape, and (2) the hexagon.

2.2 Neural network model

Based on the extensive literature review, two types of neural network models are selected for this study: multilayer

perceptron (MLP) and radial basis function (RBF) [9, 10]. These two neural network models are employed because they are much superior to others in classification for this type of data [11, 12]. The subsequent equations are either adopted or modified from the literature for this study.

2.2.1 MLP model

Each hidden or output unit is called as a perceptron, and is a function of product of input vector and associated weight [13]. The terms used in the MLP model are given as follows [9, 10]: y_i = output units, x_j = input units, w_{ij} = weights, $E(t)$ = error term in network, p = a number of training patterns, M = a number of output units, η = the learning rate between (0, 1), and $\propto$ = momentum constant.

$$Y_i = f\left(\sum_{j=1}^{n} w_{ij}x_j + b_i\right) \tag{3}$$

We use a gradient descent method for error function to find the correct weights [14]. The errors are local to each node and change in weight from node *i* to output *j*. w_{ji} is controlled by the input travels along the connection and error signal from output *j*.

$$\Delta w_{ji} = (t_i - y_i)x_i \tag{4}$$

Using the gradient descent method, the error term is propagated back through the model. The algorithm that helps in performing this is called as back propagation algorithm [15]. It has two passes: the forward pass and the backward pass. The forward pass computes functional signals and helps propagate input patterns through the network. Backward pass computes error signals and propagates the error backwards through the network starting at output units. During the backward pass, the error signal is propagated forwards. We use the normal error term, which is a sum of squares [9, 10]:

$$E(t) = \frac{1}{2}\sum_{k=1}(d_k(t) - y_k(t))^2 \text{ s} \tag{5}$$

where d_k = target value for dimension k. Gradient descent method is used to modify weights for both hidden units and output units [5-6]:

$$w_{ij}(t+1) - w_{ij}(t)\alpha - \frac{\partial E(t)}{\partial w_{ij}(t)} \tag{6}$$

The weight transformation functions for hidden units and output units, respectively, are given by [9, 10]:

$$v_{ij}(t+1) - v_{ij}(t) = \eta\delta_i(t)x_j(t);$$

$$w_{ij}(t+1) - w_{ij}(t) = \eta\Delta_i(t)z_j(t) \tag{7}$$

where the learning rate = ($0 < \eta \leq 1$). The algorithm is repeated until the stopping criterion is achieved. Stopping criterion for the network is given by [9, 10]:

$$E = \sum_{i=1}^{p}\sum_{j=1}^{M}(d_k(t) - y_k(t))^2 \tag{8}$$

where p = a number of training patterns, and M = a number of output units.

2.2.2 RBF model

In radial basis function, the Euclidean distance is computed from the point being evaluated to the center of each neuron [16]. A radial basis function (also called a kernel function) is applied to the distance to compute the weight (influence) for each neuron, such that *Weight* = RBF (*distance*). Various functions can be used as activation functions for RBF networks [17, 18]. However, for the pattern classification, Gaussian function is preferred over others. The Gaussian activation function for RBF network is given by [9, 10]:

$$\phi_j(X) = \exp\left[-(X - \mu_j)^T\sum_{j}^{-1}(X - \mu_j)\right] \tag{9}$$

where X = input feature vector, L = a number of hidden units, W = network weights, d_j = associated value of desired output, $\emptyset_j(X)$ = Gaussian activation function, and μ_j and $\sum_j^{-1}(X - \mu_j)$ = mean and covariance of the matrix of the j^{th} Gaussian function, and j = 1, 2, … , L. The output layer is a weighted sum of hidden unit outputs [9, 10]:

$$\psi_k(X) = \sum_{j=1}^{L}\lambda_{jk}\varphi_k(X)$$

$$Y_k(X) = \frac{1}{1 + \exp[-\psi_k(X)]} \tag{10}$$

where λ_{jk} = the output weights, each corresponding to the connection between hidden unit and output unit. M represents a number of output units. Using the generalized RBF network, take the condition number of matrix as a ratio of the largest Eigen value to the smallest Eigen value of the matrix. Haykin [9] states that a reduction of complexity of network is necessary to overcome the computational difficulties. The approximation procedure is used to find out the sub-optimal solution from Galerkin's method in variation problems. According to this technique, the approximation solution on finite basis is [9, 10]:

$$F(x) = \sum_{i=1}^{M} w_i\varphi_i(X) \tag{11}$$

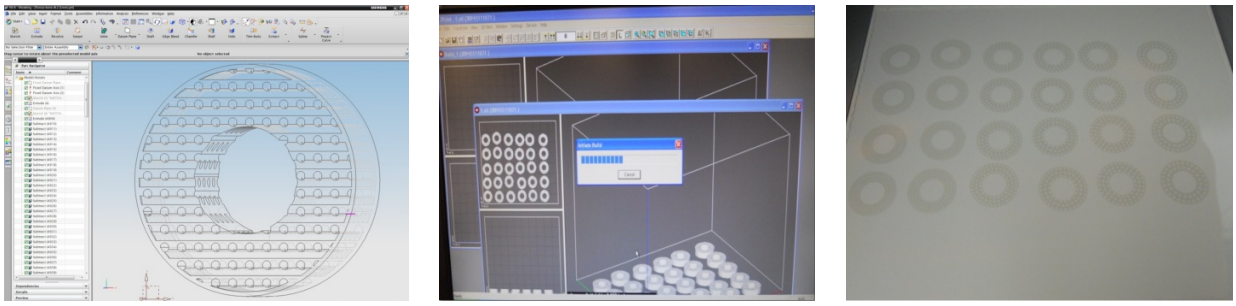

(a) (b) (c)

Figure 1. Preparation of model building using a 3D printer: (a) screen shot of scaffolds model in UGS NX 6.0, (b) 3D print Z450 preparation, (c) 3D printer making prints of scaffold models.

where $\varphi_i(X)$, i = 1,2…M, is a new set of basis functions, which are assumed to be linearly dependent. Considering RBFs, Haykin [9] gives the following equation:

$$\varphi(X) = G\left(\left\|x - t_i\right\|\right), \quad i = 1,2 \ldots M \tag{12}$$

It can be rewritten as:

$$F(X) = \sum_{i=1}^{N} w_i G(X;t_i) = \sum_{i=1}^{N} w_i G\left(\left\|x - t_i\right\|\right) \tag{13}$$

Then, the equation can be rephrased as squared Euclidean norm [19]:

$$Euclidean\ Norm\ =\ \left\|d - GW\right\|^2 \tag{14}$$

where $d = [d_1, d_2, \ldots . d_N]$. From this equation, one can find out the desired output and weights, where G is a matrix of green functions and W is a matrix of weight vectors.

3. Design and fabrication of 3D scaffolds

The design drawing of scaffold is modeled using UGS NX 6.0 software. Several models of scaffolds are drawn with varying pore sizes (0.5 mm ~ 1 mm) and shapes (circle and hexagon). The models are converted into stereo lithography files for 3D printing. Figure 1 shows the screenshot of scaffold model and the actual building process. These files are imported to the 3D Printer (Z450) software for production. Once produced, the powders are removed and the samples are put on the inspection station consisting of a robot, a conveyor and a machine vision system. The sample dimensions are analyzed using the machine vision system. The sample under inspection is checked with the image processing and analysis algorithms. Then, sample dimensions are measured and stored. The machine vision system gives signals to the robot, either to keep samples or reject.

In this study, the vision sensors and the robot are integrated to classify the quality of bone scaffolds in an automated way. This is a unique aspect of this study, because the remote connectivity of robot-vision system allows the users to monitor and carry out the inspection from a remote site. The robot has an onboard Ethernet board for Internet access, while the vision system can be remotely accessed as well. The network-connected vision-robot inspection provides an efficient and ubiquitous way of inspection, classification, and quality control of bone scaffolds. The vision inspection was mainly carried out using the various Filters and image analysis algorithms, which are provided by the software. For the surface feature analysis, the provided image tools were deemed adequate, which produced accurate results. The boundary of each pore is separated from the background pixels, and the calibrated pixel sizes are applied to attain the actual pore dimensions as well as the distance between the pores. The detailed image analysis techniques have been intensely studied in other studies by the authors. At the same time, the vision-robot system installed at the University of Texas at El Paso has been well described in other studies [20, 21]. Therefore, no further elaboration is given in this paper. Figure 2 shows the vision inspection screen.

Overall, a total of 134 samples are printed. The pores are produced from 0.5 mm to 1 mm with an increment of 0.1 mm. Therefore, there are six cases of each. Figures 3 and 4 show variations in the scaffold pore size for both hexagonal and circular shapes. The sample measurement data are shown in Table 1. For each category of *R*, *D*, *PN*, *SA*, *P*, and *S*, the maximum and minimum values are indicated as bold faced numbers.

4. Data analysis

4.1 Classification analysis with MLP & RBF

Making decision as the categorical target (good or bad) and the factors in analysis like radius, shape, distance, surface area, porosity and a number of pores as continuous inputs have been considered in the analysis. The data are analyzed using three fold testing and validation [15]. Software enables users to give the network minimum and maximum weight decay for the hidden neurons and output neurons. Also, users can specify the mode of analysis: train, test or validation [11]. For MLP, a range of networks from 3 to 50 was analyzed, and an overall accuracy of 100% has been achieved with training. For RBF, a range of networks from 14 to 50 was analyzed, and an overall accuracy of 100% has been achieved with training.

Table 1. Sample data (*R*: radius, *D*: distance between pores, *PN*: pore numbers, *SA*: surface area, *P*: porosity, *S*: shape, 1 being hexagonal and 2 being circular).

No.	R	D	PN	SA	P	S	No.	R	D	PN	SA	P	S	No.	R	D	PN	SA	P	S
1	0.9195	4.12	94	2.656	0.7064	1	46	0.882	4.02	102	2.4442	0.7053	1	91	0.8045	2.77	108	2.0335	0.6213	2
2	0.9215	3.89	94	2.668	0.7095	1	47	0.969	4.3	102	2.9502	0.8513	1	92	0.8035	2.83	112	2.0285	0.6427	2
3	0.9415	4.56	94	2.785	0.7406	1	48	0.968	4.23	93	2.9441	0.7746	1	93	0.798	2.53	107	2.0008	0.6056	2
4	0.8815	4.54	94	2.441	0.6492	1	49	0.9625	4.07	94	2.9107	0.7740	1	94	0.675	2.5	70	1.4315	0.2835	2
5	0.9235	**4.97**	94	2.679	0.7126	1	50	0.9315	2.9	61	2.7262	0.4704	1	95	0.6475	2.1	116	1.3173	0.4322	2
6	0.911	4.14	102	2.6076	0.7524	1	51	0.8825	2.54	69	2.4470	0.4776	1	96	0.627	2.1	54	1.2352	0.1887	2
7	0.867	4.05	102	2.3618	0.6815	1	52	0.866	2.87	80	2.3563	0.5333	1	97	0.578	2.03	71	1.0496	0.2108	2
8	0.855	4.4	102	2.2968	0.6627	1	53	0.8605	2.5	88	2.3265	0.5792	1	98	0.5765	2.14	84	1.0442	0.2481	2
9	0.9205	4.02	102	2.6622	0.7682	1	54	0.892	2.83	70	2.4999	0.4950	1	99	0.54	2.18	62	0.9162	0.1607	2
10	0.903	4.3	102	2.562	0.7393	1	55	0.8625	2.71	84	2.3373	0.5554	1	100	0.5565	2.09	58	0.9730	0.1596	2
11	0.9085	4.23	93	2.5933	0.6823	1	56	0.871	3.05	62	2.3836	0.4180	1	101	0.545	2.25	70	0.9332	0.1848	2
12	0.9035	4.07	94	2.5648	0.6820	1	57	0.82	2.42	92	2.1126	0.5498	1	102	0.5975	2.05	81	1.1217	0.2570	2
13	0.9015	2.9	61	2.5535	0.4406	1	58	0.8225	2.71	103	2.1255	0.6193	1	103	0.5225	2.15	76	0.8577	0.1844	2
14	0.8685	2.54	69	2.3699	0.4626	1	59	0.8005	2.1	113	2.0133	0.6436	1	104	0.9725	3.16	82	2.9715	0.6893	2
15	0.8645	2.87	80	2.3482	0.5314	1	60	0.8375	2.08	106	2.2038	0.6608	1	105	**1.0465**	3.44	75	**3.4409**	0.7301	2
16	0.877	2.5	88	2.4166	0.6016	1	61	0.8355	2.42	76	2.1933	0.4715	1	106	1.0205	3.19	87	3.2721	0.8053	2
17	0.8955	2.83	70	2.5196	0.4989	1	62	0.821	2.72	109	2.1178	0.6530	1	107	0.995	3.48	86	3.1106	0.7568	2
18	0.8705	2.71	84	2.3809	0.5658	1	63	0.649	2.42	113	1.3234	0.4230	1	108	0.978	3.24	83	3.0052	0.7056	2
19	0.8825	3.05	62	2.4470	0.4292	1	64	0.6375	2.35	83	1.2769	0.2998	1	109	0.898	2.89	110	2.5337	0.7884	2
20	0.8005	2.42	92	2.0133	0.5240	1	65	0.6325	2.69	116	1.2569	0.4125	1	110	0.8855	2.54	104	2.4636	0.7248	2
21	0.8005	2.71	103	2.013	0.5866	1	66	0.6005	2.4	71	1.1335	0.2275	1	111	0.8665	2.45	107	2.3590	0.7141	2
22	0.8105	2.1	113	2.0640	0.6598	1	67	0.6335	2.23	**127**	1.2609	0.4530	1	112	0.8795	2.91	111	2.4304	0.7632	2
23	0.822	2.08	106	2.1229	0.6366	1	68	0.6475	2.12	81	1.3173	0.3018	1	113	0.897	2.9	97	2.5280	0.6937	2
24	0.775	2.42	76	1.8871	0.4057	1	69	0.515	2.09	73	0.8333	0.1721	1	114	0.8615	2.54	112	2.3319	0.7388	2
25	0.845	2.72	109	2.2434	0.6918	1	70	0.5255	1.95	65	0.8676	0.1595	1	115	0.8615	2.51	120	2.3319	0.7916	2
26	0.6005	2.42	113	1.1330	0.3622	1	71	0.53	**1.87**	64	0.8825	0.1598	2	116	0.868	2.59	123	2.3672	0.8237	2
27	0.62	2.35	83	1.2077	0.2836	1	72	0.61	2.3	110	1.1691	0.3638	2	117	0.91	2.64	122	2.6018	0.8980	2
28	0.617	2.69	116	1.1961	0.3925	1	73	0.575	2.14	**50**	1.0388	0.1469	2	118	0.878	2.58	121	2.4221	0.8291	2
29	0.6435	2.4	71	1.3010	0.2613	1	74	0.9765	3.16	82	2.9960	0.6950	2	119	0.916	2.75	121	2.6363	**0.9024**	2
30	0.6785	2.23	127	1.4464	0.5196	1	75	1.018	3.44	75	3.2561	0.6908	2	120	0.836	2.56	105	2.1959	0.6523	2
31	0.64	2.1	107	1.2869	0.3895	1	76	0.9735	3.19	87	2.9776	0.7328	2	121	0.82	2.77	108	2.1126	0.6455	2
32	0.6975	2.12	81	1.5286	0.3502	1	77	0.974	3.48	86	2.9807	0.7252	2	122	0.8025	2.83	112	2.0234	0.6411	2
33	0.51	2.09	73	0.8172	0.1687	1	78	0.9665	3.24	83	2.9350	0.6891	2	123	0.821	2.53	107	2.1178	0.6410	2
34	0.575	1.95	65	1.0388	0.1910	1	79	0.8785	2.89	110	2.4248	0.7546	2	124	0.7225	2.5	70	1.6401	0.3248	2
35	0.6	**1.87**	64	1.1311	0.2048	1	80	0.8875	2.54	104	2.4748	0.7281	2	125	0.6095	2.1	116	1.1672	0.3830	2
36	0.59	2.3	110	1.0937	0.3403	1	81	0.8955	2.45	107	2.5196	0.7627	2	126	0.5205	2.08	65	0.8512	0.1565	2
37	0.525	2.14	**50**	0.8660	**0.1225**	1	82	0.8935	2.91	111	2.5083	0.7876	2	127	0.645	2.1	54	1.3071	0.1996	2
38	0.9485	4.12	94	2.8267	0.7517	1	83	0.892	2.9	97	2.4999	0.6860	2	128	0.578	2.03	71	1.0496	0.2108	2
39	0.87	3.89	94	2.3781	0.6324	1	84	0.8815	2.54	112	2.4414	0.7735	2	129	0.548	2.14	84	0.9435	0.2242	2
40	0.9655	4.56	94	2.9289	0.7788	1	85	0.86	2.51	120	2.3238	0.7889	2	130	0.565	2.18	62	1.003	0.1759	2
41	0.8675	4.54	94	2.3645	0.6288	1	86	0.9045	2.59	123	2.5705	0.8944	2	131	0.58	2.09	58	1.0569	0.1734	2
42	0.9735	**4.97**	94	2.977	0.7918	1	87	0.876	2.64	122	2.4110	0.8321	2	132	**0.505**	2.25	70	**0.8012**	0.1586	2
43	0.8825	4.14	102	2.447	0.7061	1	88	0.893	2.58	121	2.5055	0.8577	2	133	0.575	2.05	81	1.0388	0.2380	2
44	0.8855	4.05	102	2.4636	0.7109	1	89	0.889	2.75	121	2.4831	0.8500	2	134	0.595	2.15	76	1.1123	0.2391	2
45	0.885	4.4	102	2.4608	0.7101	1	90	0.808	2.56	105	2.0512	0.6093	2							

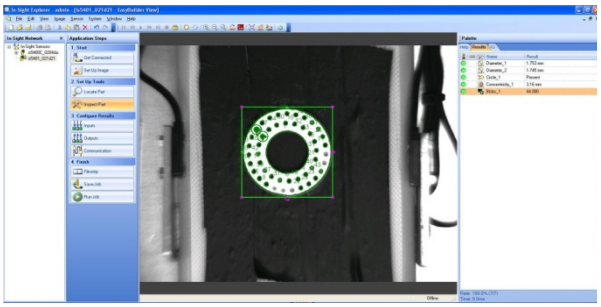

Figure 2. Screen shot of Cognex insight explorer with scaffold being investigated.

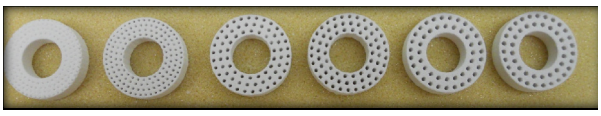

Figure 3. Hexagonal scaffolds with varying pore sizes from 0.5 mm ~ 1 mm.

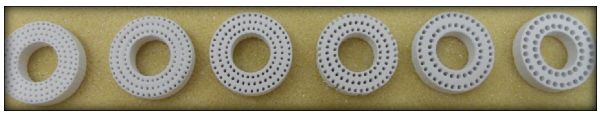

Figure 4. Circular scaffolds with varying pore sizes from 0.5 mm ~ 1 mm.

It is found that both MLP and RBF work well with the data, which result in a very high classification accuracy. According to the rule of thumb, the hidden number of layers should be within 10% of the whole data set (i.e., hidden layers for artificial neural networks should be around 11-15). This heuristic has been supported with the results. For MLP, the classification accuracy is 100% for train, test and validation data for networks in the range of 11-15. The classification accuracy in case of MLP is at the maximum for MLP 11, MLP 12, and MLP 13. Similarly, in case of RBF, the maximum classification accuracy is 100%, 100%, 96.67% for train, test and validation, respectively. For validation data set, there are 2 incorrect ensemble predictions for the maximum classification accuracy for networks RBF 25, RBF 26, and RBF 45.

4.2 Regression analysis

Regression analysis is performed to find out the effect of independent variables on the dependable variable (i.e., porosity). The error terms are compared to gauge the performance of each model.

4.2.1 Regression analysis with MLP & RBF

Using the MLP, we define the network model similar to the case of classification analysis. Instead of the whole sensitivity analysis process, the best network chosen from the classification analysis is considered for the regression model. The data are divided into three fold, where two thirds of the data is considered as a train set and the remaining as the test and validation set. Among one thirds of the data, 50% is chosen as validation and other 50% for testing. The resultant prediction from the MLP model for the output porosity is compared with the target porosity and the error term is generated. In a similar way, the regression analysis is performed with the RBF model and the target porosity is compared with the ensemble output porosity. Also, error term is generated through the network. Figure 5 shows the performance of MLP regression analysis.

4.2.2 Regression model

To find the impact of significant factors, a software package Minitab 15 is used to perform the ANOVA test and the regression analysis using the experimental data from Table 1. Note that the maximum difference between the actual and predicted values is bold-faced in Table 1. Among the 5 factors considered include the size, shape, distance, a number of pores and surface area. The analysis shows the effect of each factor independently and interaction between factors on the model. We observed from the ANOVA test that the effects of all five factors on porosity are significant and interactions are significant as well. To develop the regression model, we performed a fractional factorial design for the given case. Considering a half factorial design, the possible number of experiments is $2^{n-1}$and the total number of scaffolds that needed to be analyzed is 16. The order of 16 experiments is randomized. The regression model is given by:

$$\begin{aligned} Porosity(Y) &= 0.52635 + 0.15136*R + 0.03465*D + \\ &0.08097*PN + 0.04166*S - 0.02108*SA - 0.0422*R*PN + \\ &0.01727*R*S - 0.01917*D*S - 0.04906*D*SA + \\ &0.02654*PN*S + 0.01653*S*SA \end{aligned} \quad (15)$$

where R = radius, D = distance between pores, PN = pore numbers, SA = surface area, P = porosity, S = shape, 1 being hexagonal and 2 being circular. The adjusted R-square value is 90.25%, which shows a very good fit with the 16 data points that were used for the model development. We observed that a maximum porosity is obtained when radius, distance between pores, a number of pores, and shape is high. From the results, the error term is at the lowest with MLP, which is 0.000001. This network model is built so strong that the testing accuracy, training accuracy and validation accuracy are almost 100%. The RBF results are comparable with the regression model, which show slight more variations. Figure 6 shows comparison between the actual porosity values and the predicted values from the regression model.

5. Conclusions

This research features the following contributions. First, the parameters involved in fabrication of scaffold are considered simultaneously. Second, the classification analysis is performed for parameters under consideration to obtain the categorical target of Good/Bad for the scaffolds prepared. A

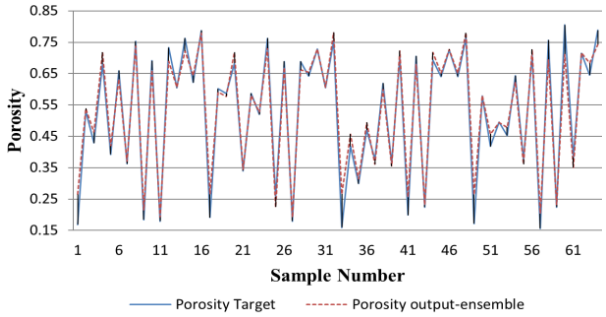

Figure 5. Regression analysis for MLP model.

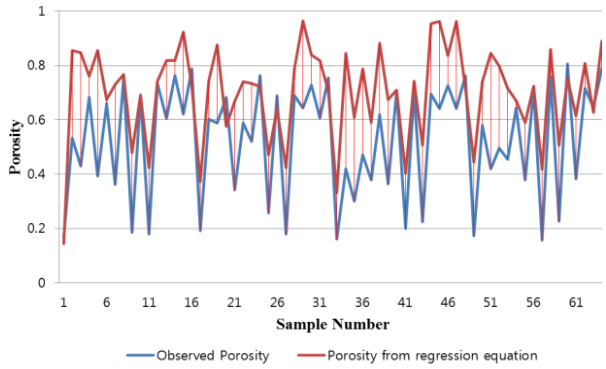

Figure 6. Comparison between the actual and predicted porosity values.

non-linear regression model and neural network models involving back propagation algorithms are used to estimate the uncertainty. Third, the error terms predicted by the models are compared with experimental data. Two new models are designed using MLP and RBF neural networks because of its advantages in classification and regression. From the analysis, the MLP model shows a 100% classification accuracy, while the RBF shows the classification accuracy of 96.67%.

To predict the porosity, a regression model was developed using a design of experiments. All five factors that are used in this design are proved significant in terms of predicting the porosity. In this regard, the neural network models performed better than the regression model. The MLP has the lowest error term in predicting the porosity. The results prove the significance of each independent factor on the regression model, which can be observed from a response optimizer. It shows that a radius of pores should be high, a number of pores should be high, a hexagonal shape is better, and the distance between pores should be large as well. The results prove that a hexagonal shape is better than a circular pore because it has more edges and can be better suited for cell culturing.

Acknowledgments

This research was supported by the Basic Science Research Program through the National Research Foundation of Korea (NRF) funded by the Ministry of Education (Grant No. NRF-2013R1A1A2006108) and the National Science Foundation (DUE-TUES-1246050). The authors wish to express sincere gratitude for their financial support.

References

[1] Ma PX, Elisseeff J. Scaffolding in tissue engineering. Boca Raton(FL): CRC Press; 2006. 656 p.

[2] Dietmar H. Scaffolds in tissue engineering bone and cartilage. Biomaterials. 2000; 21(24): 2529-2543.

[3] Zein I, Hutmacher DW, Tan KC, Teoh SH. Fused deposition modeling of novel scaffold archtectures for tissue engineering applications. Biomaterials. 2002; 23(4): 1169-1185.

[4] Liu X, Ma PX. Polymeric scaffolds for bone tissue engineering. Annals of Biomedical Engineering. 2004; 32(3): 477-486.

[5] Gbureck U, Holzel T, Biermann I, Barralet JE, Grover LM. Preparation of tricalcium phosphate/calcium pyrophosphate structures via rapid prototyping. Journal of Material Science: Materials in Medicine. 2008; 19(4): 1559-1563.

[6] Leukers B. Hydroxyapatite scaffolds for bone tissue engineering made by 3D printing. Journal of Materials Science: Materials in Medicine. 2005; 16(12): 1121-1124.

[7] Khalyfa A, Vogt S, Weisser J, Grimm G, Rechtenbach A, Meyer W, Schnabelrauch M. Development of a new calcium phosphate powder- binder system for 3D printing of patient specific implants. Journal of Materials Science: Materials in Medicine. 2007; 18(5): 909-916.

[8] Sherwood JK, Rileyb SL, Palazzoloa R, Browna SC, Monkhousea DC, Coatesc M, Griffithc LG, Landeenb LK, Ratcliffe A. A three dimensional osteochondral composite scaffold for articular cartilage repair. Biomaterials. 2002; 23(24): 4739-4751.

[9] Haykin S. Neural Networks: A Comprehensive Foundation. New Jersey (NJ), Prentice Hall PTR; 1994. 716 p.

[10] Feraud R, Fabrice C. A methodology to explain neural network classification. Neural Networks. 2001; 15(2): 237-246.

[11] Leite E, Carlos R. TEXTNN–a matlab program for textural classification using neural networks. Computers and Geosciences. 2009; 35(10): 2084-2094.

[12] Chen L, Wei X, Naoyuki T. Classification of 2 dimensional array patterns: assembling many small neural networks is better than using a large one. Neural Networks. 2010; 23(6): 770-781.

[13] Arulampalam G, Abdesselam B. A generalized feed forward neural network architecture for classification and regression. Neural networks. 2003; 16(5): 561-568.

[14] Kraipeerapun P, Chun C. Binary classification using ensemble neural networks and interval neutrosophic sets. Neurocomputing. 2009; 72(13): 2845-2856.

[15] Kavzoglu T. Increasing the accuracy of neural network classification using refined training data. Environmental Modelling & Software. 2009; 24(7): 850-858.

[16] Casasent D, Chen XW. Radial basis function neural network for non-linear Fisher discrimination and Neyman-Pearson classification. Neural Networks. 2003; 16(5-6): 529-535.

[17] Korurek M, Berat D. ECG beat classification using particle

swarm optimization and radial basis function neural network. Expert System with Applications. 2010; 37(12): 7563-7569.

[18] Ng WWY, Dorado A, Yeung DS, Pedrycz W, Izquierdo E. Image classification with the use of radial basis function neural networks and the minimization of the localized generalization error. Pattern Recognition. 2007; 40(1): 19-32.

[19] Park S, Hwang JP, Kim ET, Lee HJ, Jung HG. A neural network approach to target classification for active safety system using microwave radar. Expert System with Applications. 2010; 37(3): 2340-3246.

[20] Kwon Y, Park Y. Improvement of vision guided robotic accuracy using Kalman filter. Journal of Computers & Industrial Engineering. 2013; 65(1): 148-155.

[21] Kwon Y, Hong J. Integrated remote control of the process capability and the accuracy of vision calibration. Journal of Robotics & Computer Integrated Manufacturing. 2014; 30(5): 451-459.